Solar Energy 303 (2026) 114115

Contents lists available at ScienceDirect

Solar Energy

journal homepage: www.elsevier.com/locate/solener

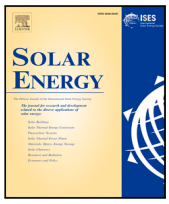

Solar concentrator layout and performance analysis for multi-aperture receiver-reactors in high-temperature applications

Hanna Lina Pleteit [a,b,*], Stefan Brendelberger [a], Peter Schwarzbözl [c], Malou Großmann [a], Martin Roeb [a], Christian Sattler [a,b]

[a] Deutsches Zentrum für Luft- und Raumfahrt e.V. (DLR), Future Fuels, Linder Höhe, Cologne, 51147, Nordrhein-Westfalen, Germany
[b] Rheinisch-Westfälische Technische Hochschule (RWTH) Aachen, Chair of Solar Fuel Production, Templergraben 55, Aachen, 52062, Nordrhein-Westfalen, Germany
[c] Deutsches Zentrum für Luft- und Raumfahrt e.V. (DLR), Solar Research, Linder Höhe, Cologne, 51147, Nordrhein-Westfalen, Germany

ARTICLE INFO

Keywords:
Multi-aperture receiver
Heliostat field
Central receiver system
Solar thermochemical water splitting
Concentrated solar power

ABSTRACT

Promising new receiver-reactor concepts with multiple apertures have been proposed for high temperature solar thermochemical hydrogen production. However, limited information about suitable solar concentrator designs consisting of heliostat fields and secondary concentrators is available so far.

The goal of this study is a detailed investigation of the effect of selected solar concentrator design parameters on its performance. For a 10 MW receiver-reactor the number of subfields and corresponding apertures is varied in combination with the receiver height above the ground, the acceptance angle of the secondary concentrator, and the design point flux density. In addition, the performance is analyzed at different power levels. The average annual performance is evaluated as well as the hourly behavior. The latter of which is important to quantify the performance of a plant with an integrated receiver-reactor.

For the heliostat field layout the program HFLCAL[1] is used. Solar concentrator designs with annual average efficiencies of over 60% are identified delivering flux densities of up to 5000 suns at design point for 10 MW receivers. Instead of a joint evaluation of the solar concentrator together with a specific receiver-reactor a generic receiver-reactor surrogate model is introduced. With this surrogate model an hourly analysis of the plant performance is conducted and a parametrized correction factor is presented to derive more accurate yearly plant performance estimates.

The study provides detailed information on solar concentrators using multiple heliostat subfields and central tower systems with secondary optics, and indicates further optimization potential of solar concentrators for high-temperature receivers.

1. Introduction

Solar thermochemical redox cycles for water splitting are considered as a promising production method for renewable hydrogen with high efficiency and good scaling potential [1]. Thereby, receiver-reactors use highly concentrated solar radiation to run endothermic reactions at high temperatures. In recent years mainly receiver-reactors applying ceria as redox material have been proposed. For this redox cycle receiver-reactor temperatures of 1500 °C and more are considered [2]. To limit the radiative heat losses through the aperture of the receiver-reactor, high flux densities in the order of several thousand suns delivered by the solar concentrator are required. The optimization of a solar thermochemical plant, including the solar concentrator and receiver-reactor, requires detailed information about both sub-systems. For parametrized solar concentrator and receiver-reactor models the objective function becomes highly multi-model making the search for a global optimum difficult [3]. Therefore, the sub-systems are often evaluated and optimized independently during initial performance investigations.

Central receiver systems (CRS) with heliostat fields can provide high flux densities at large scale required for high-temperature processes. Secondary concentrators are technically challenging, but might be required to further increase the flux density as used in [3–6]. The most common secondary concentrator is the compound parabolic concentrator (CPC). The CPC's concentration factor increases for smaller CPC acceptance angles. At the same time, the acceptance angle limits the

* Corresponding author.
E-mail address: hanna.pleteit@dlr.de (H.L. Pleteit).

[1] Heliostat Field Layout CALculation software (version dated 4th of July 2024).

https://doi.org/10.1016/j.solener.2025.114115
Received 22 May 2025; Received in revised form 24 October 2025; Accepted 27 October 2025
Available online 3 November 2025

view cone of the CPC, which is the area on the ground where heliostats can be placed and beyond which there is a steep drop off in accepted light [7]. CRS, usually without secondary optics, have been developed for concentrating solar power (CSP) plants and are already at a commercial level. Typical flux densities for Rankine-based CSP plants are in the order of 500 to 1000 suns [8] and corresponding solar concentrator designs have been investigated in detail in the past for power plants at several hundred MW of power reaching the receiver [4,6]. For high-temperature processes often smaller CRS in the range of 10 MW to 100 MW are considered, which can be combined to multi-tower systems in order to increase the total power [9].

Schmitz et al. [4] proposed multi-aperture thermal receiver systems with secondary concentrators as an alternative to polar and surround fields for large CRS. They analyzed the optical efficiency as a function of the power level for design point receiver power levels between 10 MW and 400 MW. Important information for the evaluation of solar thermochemical processes like the flux density at the aperture is not provided. Pitz-Paal et al. [3] optimized solar field layouts for high-temperature solar thermochemical processes. In the study, optimized heliostat fields have been identified for three processes (zinc dissociation, coal gasification, and a thermal receiver) at three different power levels (1 MW, 10 MW, and 100 MW) for fixed tower heights, but multiple apertures are only considered at the highest power level. Even though the results are relevant for the ceria cycle discussed here, the information in the study is limited and it is only possible to derive very simple estimates of the solar concentrator performance for the high-temperature processes targeted here. In particular the performance at different design point flux densities is only provided for two values per power level. Brendelberger et al. [10] investigated solar field configurations with multiple apertures, receiver-reactor arrays, and secondary optics for a solar thermochemical ceria receiver-reactor based on the SUN-to-LIQUID design [11]. Due to the batched operation of this receiver-reactor, the heliostats are pointing to different apertures during the cyclic operation. Only moderate concentration factors of 2500 suns have been targeted and solar concentration efficiencies of up to 55% have been obtained. For larger power levels (30 MW & 50 MW), multiple heliostat fields have been considered. The yearly distribution of flux densities are provided, but the study is limited to the SUN-to-LIQUID receiver-reactor. Li et al. [6] present a field optimization study for multi-aperture CRS for high-temperature applications. Maximum annual solar-to-thermal efficiencies are provided for receiver temperatures between 600 K and 1800 K and for receiver power levels up to 500 MW. They investigated the influence of the number of different sub-fields and the effect of the optical properties of reflective surfaces. In general, the study is relevant for the work presented here and results for a large number of cases are provided. Still, information is missing to derive the optical performance on an hourly basis which is necessary to evaluate the solar concentrator in combination with different receiver-reactors. A study by Daniel Potter et al. [12] addresses multi-aperture falling particle receivers but is limited in scope providing only data for 50 MW and 500 MW systems and three tower heights comparing one and three apertures.

In total, only limited information about solar concentrators that provide high enough flux densities for solar thermochemical cycles is available and it is difficult to derive accurate performance metrics for new receiver-reactors based on the available information. As a result, in thermodynamic solar thermochemical plant and techno-economic studies the performance of the solar concentrator is often not considered at all or by rough efficiency estimates [13,14].

The goal of this study is to fill this gap and to provide information about solar concentrators which can be used to assess high-temperature receiver systems in general. It particularly aims to identify optimal solar concentrator designs for systems like the recently published new receiver-reactor concept of type R2Mx (receiver-reactor cavity system with multiple mobile redox units) [15] with multiple apertures and corresponding subfields. Due to the lack of more detailed information in literature, the solar field performance is approximated in the cited study by a two-point correlation between flux density and annual average optical efficiency based on Pitz-Paal et al. [3]. Furthermore, the annual average plant efficiency is therein calculated based on the annual average solar concentrator performance and the receiver-reactor design point value, which is most likely overestimating the performance in comparison to a time resolved performance estimation based on time-resolved flux densities. The study presented here is intended to provide more detailed information about promising solar concentrator designs and to allow to evaluate the potential of plant performances based on hourly data.

Thereto, a parameter study of a solar concentrator for a 10 MW receiver-reactor system is provided varying the design point flux density (given as the concentration factor C), the number of apertures and corresponding heliostat subfields, the receiver height above ground and the CPC acceptance angle. The aperture tilt angle and the heliostat positions are optimized with respect to the maximum annual average efficiency of the respective subfields. Furthermore, the solar concentrator is assessed at different power levels (7.5 MW and 20 MW) to investigate the scaling behavior. All simulations conducted are based on the HFLCAL modeling code [16]. An approach using a generic receiver-reactor surrogate model and correction factors is introduced to approximate plant performances based on hourly data by the correction of design point estimates, potentially reducing substantially the effort for future plant performance studies. In total, the presented study provides the necessary information about solar concentrators to evaluate and optimize in more detail fuel production plants comprising solar concentrator and high-temperature receiver-reactor.

2. Materials and methods

The data for this study is generated using dedicated models of the different parts of a solar plant. Section 2.1 describes the model for the solar concentrator, which is complemented by Section 2.2 with a description of the heliostat field layout program HFLCAL. The setup of the parameter study is then described in detail in Section 2.3. Finally, a generic receiver-reactor surrogate model is introduced in Section 2.4 in order to quantify the resulting plant performance.

2.1. Solar concentrator model

For the model of a solar concentrator a heliostat field together with a tower is modeled. The tower model contains a receiver with multiple apertures, each with a CPC as secondary concentrator. The heliostat field is divided into a number of subfields corresponding to the number of apertures. Only subfields in the western half of the total field perimeter are simulated due to the east–west symmetry in the heliostat field [6]. The entry point for the model is the sunlight intercepted by the heliostat surfaces and the exit point is the beam intercepted by the receiver apertures. The result is an annual performance which consists of the fraction of sunlight falling onto the heliostats that is intercepted by the receiver apertures.

The programme HFLCAL is used to calculate the annual performance values based on the hourly performance of the 21st of every month as a representative day. It takes into account the Sun's position, cosine losses, atmospheric attenuation, shading and blocking and imperfections in the heliostat and CPC mirrors. To choose the most efficient heliostat field layout HFLCAL starts with an oversized distribution of heliostats for each of which the annual performance is calculated. HFLCAL then includes the best performing heliostats until the design point intercepted power at the design date (in this study: 21st of March 12:00 solar time) is reached. The method is illustrated in Pitz-Paal et al. [3]. Schmitz et al. [4] validated this approach by comparing the loss and efficiency values for one specific field configuration to a more elaborate and computationally expensive simulation based on ray-tracing.

On top of this, a genetic algorithm optimizes the field layout parameters on which the heliostats' starting distribution depends along with the CPC tilt angle, which is the angle between the horizontal and the optical axis of the CPC, for maximizing the annual average efficiency. Further detail on the genetic optimization can be found in Pitz-Paal et al. [3]. The field layout optimization is done for every subfield independently by simulating a single aperture field in the way explained above with field limits that constrain the field to its respective circle segment. For simplification, the subfields are non-overlapping and each heliostat only belongs to one subfield and can only reflect light onto one aperture (see Fig. 1).

For this study it was decided to set the receiver-reactor inlet design point power to 10 MW for the base case. This is small compared to existing concentrating solar tower plants but still at a commercially relevant scale. The choice is motivated by the unusual high flux densities of the system targeted in this study, which are expected to lead to strongly decreasing optical efficiencies at larger scale. The importance of high flux densities becomes clear in the discussion of the receiver-reactor performance analysis 2.4. For larger overall power levels, the use of multi-tower systems seems promising as it was already proposed in similar contexts [11]. Furthermore, since commercially available windows suitable to cover the aperture are limited in size, it was decided to use at least three apertures over which the power is distributed, keeping the size of the single apertures at a realistic level.

Another important assumption is that the design point flux density and power are the same in at each aperture. This design choice is considered a reasonable simplification, since otherwise optimal receiver-reactors designs would also depend on the orientation of each receiver-reactor and vary within the same plant - increasing the complexity significantly. Furthermore, receiver-reactors like R2Mx are expected to benefit from a rather homogeneous flux distribution [15]. In general, dropping this restriction is expected to allow further optimization of a plant. To limit the influence of the assumption in this study, the location of the heliostat field is chosen to be in between the solar tropics. More information on the location is given in Section 2.3.

2.2. Theoretical background of HFLCAL

The theoretical background of HFLCAL is briefly summarized in this section. For a detailed description of the simulation program see Schwarzbözl et al. [16].

The Heliostat Field Layout CALculation software (HFLCAL) considers all relevant effects occurring on the way from the heliostat to the receiver. First of all, the cosine loss is calculated from the angle between the heliostat aim point on the receiver and the Sun position. Then blocking and shading losses are modeled by projecting the contours of a group of neighboring heliostats onto each heliostat and calculating the overlapping regions. The tower shadow is also considered. The atmospheric attenuation of the reflected radiation is modeled as a function of the distance between heliostat and receiver [17].

HFLCAL speeds up the simulation process by assuming that the flux distribution of the reflected beam of each heliostat can be modeled as a circular Gaussian with a dispersion given by[2]:

$$\sigma_{\text{tot}} = \sqrt{\sigma^2_{\text{sunshape}} + (2 \cdot \sigma_{\text{slope}})^2 + (2 \cdot \sigma_{\text{track}})^2} \tag{1}$$

This assumption can be justified by the central limit theorem, which states that the sum of multiple non-Gaussian distributions becomes increasingly Gaussian, especially if one of the distributions is already Gaussian, as is the case for the mirror surface error σ_{slope} (see Johnston [19]). The tracking error σ_{track} is caused by the stepwise mechanical movement of the heliostat mirror about two axes with gear backlash and bearing clearances. Mirror slope and tracking errors are usually expressed with reference to the mirror normal so they need to be considered twice.

Additionally, the reflected beam from a mirror is distorted through off-axis reflection, i.e. when the incidence angle is >0. This is accounted for in HFLCAL as a further broadening of the circular beam. For the sunshape a narrow Gaussian [16] shape with $\sigma_{\text{sunshape}} = 2.09$ mrad independent of the DNI is assumed as suggested by measurements at the DLR [20]. Hottel's clear sky model is used for calculation of the direct normal irradiance (DNI) depending on location, date and time [21].

Further, all reflectivities are assumed constant over time and include reductions to account for soiling and out-of-service heliostats. Dynamic effects on the beam shape e.g. mirror deformation by wind are not taken into account. In this study all heliostats are aimed at the center of the aperture which is justified as rather small apertures with secondary concentrators are considered (see Table 2).

To calculate the final intercept fraction, the heliostat flux distribution is integrated over the aperture that the heliostat field sees. When using a secondary concentrator this is the entrance aperture of the secondary:

$$\epsilon_{\text{inc}} = \frac{1}{2\pi \cdot \sigma^2_{\text{tot}}} \int_x \int_y \exp\left(-\frac{x^2+y^2}{2 \cdot \sigma^2_{\text{tot}}}\right) \mathrm{d}y \cdot \mathrm{d}x \tag{2}$$

The fraction of flux that falls outside of the aperture is called spillage ($\epsilon_{\text{spil}} = 1 - \epsilon_{\text{inc}}$) Besides setting the size of the entrance aperture, the secondary concentrator (CPC) also has a limited view cone defined by the acceptance angle . Radiation entering the CPC at incidence angles smaller than the acceptance angle is transmitted with some reflectance losses, while radiation from outside the acceptance angle is reflected back (see e.g. Welford and Winston [22]). This is modeled in HFLCAL by a transmission factor ϵ_{seco} as a function of the incidence angle which is interpolated from ray-tracing generated tables (see also [4]).

HFLCAL also offers the option to take into account the receiver efficiency, which is not used in this study ($\eta_{\text{rec}} = 1$), since the receiver model is added later by hand as described in Section 2.4. This means that the solar concentrator is not optimized for the receiver and with a specific receiver model coupled to the simulation potentially higher efficiencies are achievable at the expense of generality.

To arrive at the annual average efficiency all losses introduced above have to be taken into account. These are expressed as efficiencies defined as 1 minus the respective loss fraction. Included are the reflectivity of the heliostat mirrors ϵ_{refl}, the atmospheric efficiency ϵ_{atmo}, the cosine efficiency ϵ_{cos}, the blocking and shading efficiency $\epsilon_{\text{b\&s}}$, the transmission of the CPC ϵ_{CPC} and the intercept ϵ_{inc} given by Eq. (2). From these the radiation power in the apertures at time t and heliostat location (x, y) can be calculated via [16]:

$$P(x,y,t) = \text{DNI}(t) \cdot A_{\text{H}} \cdot \epsilon_{\text{refl}} \cdot \epsilon_{\text{atmo}}(x,y) \cdot \epsilon_{\text{cos}}(x,y,t) \cdot \epsilon_{\text{b\&s}}(x,y,t) \cdot \epsilon_{\text{seco}}(x,y) \cdot \epsilon_{\text{inc}}(x,y,t) \tag{3}$$

with the additional factors of the direct normal irradiance $DNI(t)$ and the heliostat mirror surface A_H.

The annual energy yield is then calculated by a weighted sum of the powers in Eq. (3) over all heliostat positions and for 12 × 24 representative time points over the course of the year (all hours of the 21st of each month):

$$E_{\text{aper,annual}} = \sum_{(x,y)} \sum_{t} w(t) \cdot P(x,y,t) \tag{4}$$

where the weight $w(t)$ includes the interval length and multiplicity of each representative time point [16].

Finally, the annual efficiency sets into relation the annual energy yield with the total incoming light from the Sun:

$$\epsilon_{\text{annual}} = \frac{E_{\text{aper,annual}}}{E_{\text{tot,annual}}} = \frac{E_{\text{aper,annual}}}{n_{\text{H}} \cdot A_{\text{H}} \sum_t w(t) \cdot \text{DNI}(t)} \tag{5}$$

[2] Eq. (1) is a conservative approach as the effects of the mirror and tracking errors decrease with increasing incidence angle (see Landman et al. [18]).

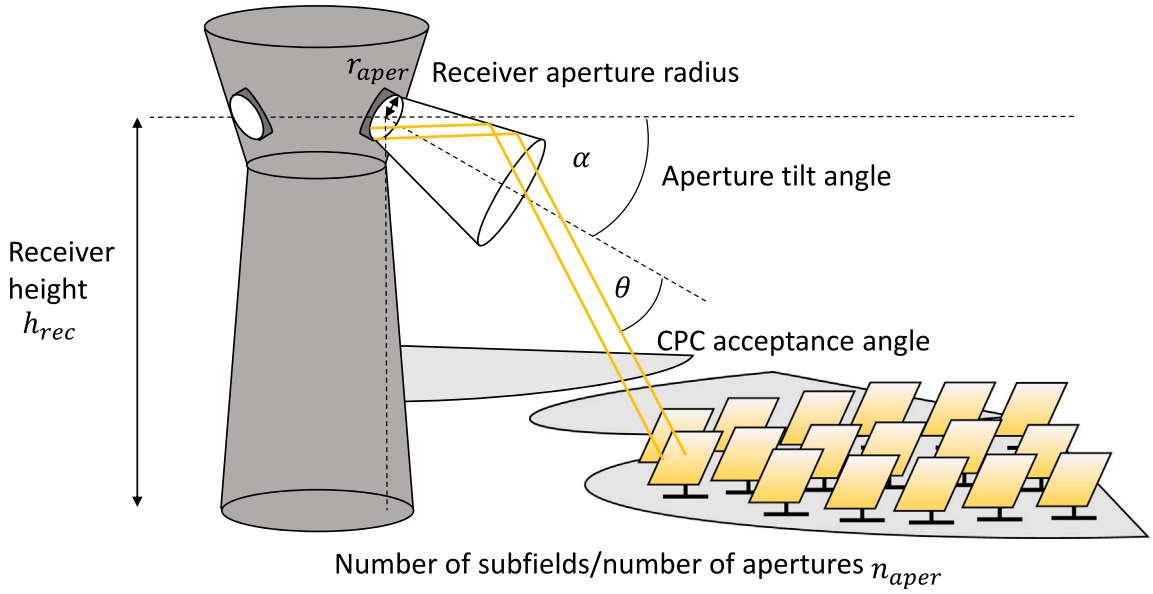

Fig. 1. Schematic representation of the receiver on the tower together with the subfields consisting of the heliostats. One exemplary CPC is shown on one of the apertures. The receiver height h_{rec} denotes the aperture center's height over the ground. The receiver aperture is further characterized by its radius r_{aper} and the tilt angle α with which the aperture is looking down from the horizontal. The CPC acceptance angle is defined with reference to the CPC's optical axis as the largest angle for which the incoming ray still falls into the aperture instead of being reflected back out of the CPC.

2.3. Parameter study

The parameter study considers a parameter space with four main parameters (i) number of subfields n_{aper}, (ii) receiver height above the ground h_{rec}, (iii) design point concentration factor C and (iv) CPC acceptance angle θ. In a subsequent step the total design point power P_{tot} is also changed.

The fixed parameters used for all simulations are given in the following. For the heliostat specifically more optimistic values for the errors are chosen to take expected improvements of the heliostat technology into account. Some sources for current values in research that are not commercially available yet are provided as well. The optical quality of the CPC is expected to be slightly less than for the heliostats:

- *Location:* Chile, latitude: 22°S, 1155 m above sea level, DNI at design point: 971.8 W/m^2
- *Environment:* cloudless sky, narrow Gaussian sunshape 2.09 mrad, flat land
- *Design date:* 21st of March, 12 am (local solar time)
- *Heliostat:* reflective area 2 m^2, square shape, one facet, perfectly focused (focal plane = entrance aperture plane of the CPC), slope error (circular normal distribution) 0.7 mrad [23], tracking error (normal) 0.6 mrad per axis [24], 96% reflectivity [25], 5% dirt on reflective surface, 1% of heliostats out of service
- *Tower:* radius = $0.05 \cdot h_{rec}$, height = $1.05 \cdot h_{rec}$
- *Receiver:* cylindrical receiver, circular apertures, aperture radius calculated from concentration factor and power (see paragraph (iii)), receiver radius = tower radius
- *CPC:* 94% reflectivity, slope error (normal) 1.5 mrad, no truncation
- *Subfields:* each subfield has the same aperture, CPC and design point power

(i) The setup of the subfields can be seen in Fig. 2. The numbering of the subfields starts with subfield number one in northern direction and growing numbers from north to west to south. The first subfield has its boundary aligned with the northern axis. The angles that the optical axis of the apertures and CPCs form with the northern axis are then given by $(360/n_{aper})/2$. The boundaries for the subfields are distributed equally and cover the whole surround field (no gap or overlap). Each heliostat is only attributed to one of the apertures so that n_{aper} distinct heliostat populations are used. This is a simplifying assumption while a possible setup with heliostats aiming at different apertures at different times of the day and year could also be imagined. However, this requires further time-dependent optimization of the combined subfields which is beyond the scope of this study. The orientation of the subfields is not varied as this was shown by Li et al. [6] to have no significant effect. The field partition is varied from three to nine subfields. A minimum of three subfields is chosen in this study as surround field configurations with preferably isotropic profile are targeted. Based on the outcome of previous studies like Li et al. [6] the efficiency is expected to decrease for a large number of subfields so that a maximum of nine is considered in this parameter study.

(ii) The receiver height h_{rec} is measured from the ground to the center of the receiver aperture. It also influences the overall tower height and radius. The height steps used for optimization are distributed around an empirical value that has been interpolated from previous solar tower plants and depends only on the total design point power P_{tot} [26]:

$$h_{rec} = 36.7\ \text{m} \cdot \left(\frac{P_{tot}}{MW} \right)^{0.288} \tag{6}$$

which yields approximately 71 m for a P_{tot} = 10 MW field. The receiver heights considered are 65 m, 75 m, 85 m and 95 m. The tilt angle of the aperture and CPC is automatically optimized by the integrated genetic optimization algorithm described in Section 2.1.

(iii) The design point concentration factor C is defined as the flux density at the receiver aperture in relation to the flux density arriving at the surface of the Earth (DNI):

$$C = \frac{P_{tot}}{\text{DNI} \cdot n_{aper} \cdot \pi r_{aper}^2} = C_{field} \cdot C_{CPC} \tag{7}$$

This is dependent on the power per receiver aperture P_{tot}/n_{aper} that changes with the number of subfields and the design point DNI that stays the same for all simulations (at design point). The concentration factor can be varied by adapting the aperture radius r_{aper}. The values for the receiver aperture radii used in the 10 MW parameter study can be found in Table 2 in Appendix. The concentration factor is varied in steps of 1000 from 2000 up to 5000.

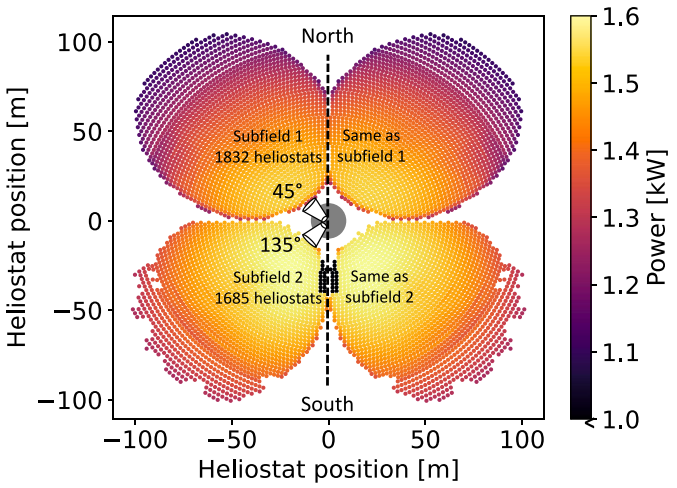

Fig. 2. One example of the result of a solar concentrator design with four subfields at 10 MW design point power. The western and eastern half are symmetric along the north–south axis. The color scale marks the power from every single heliostat that is intercepted by the respective receiver aperture. The field is shown at the design point 21st of March at solar noon. The black dots south of the tower are heliostats that do not receive light at that point in time as they are in the shadow of the tower. Holes in the subfields are a result of the tower shadow at other points in time and clearly show further potential for field design improvement. (For interpretation of the references to color in this figure legend, the reader is referred to the web version of this article.)

Eq. (7) also shows how the concentration factor can be subdivided into one contribution from the heliostat field, which contains the concentration ratio between the DNI and the entrance aperture of the CPC, and on contribution from the CPC, which is the concentration ratio between the CPC exit and entrance apertures. The last one is given by a simple geometric relation that is introduced in the next paragraph.

(iv) The acceptance angle θ limits the view cone of the CPC and affects the concentration factor of the CPC, where larger acceptance angles lead to smaller concentration factors:

$$C_{\mathrm{CPC}} = \frac{1}{\sin^2(\theta)} \tag{8}$$

By inserting Eq. (8) into Eq. (7) it becomes apparent that higher CPC concentration factors automatically lead to smaller field concentration factors in the parameter study which seems counterintuitive. However, the overall concentration factor is kept constant on purpose by fixing the total power when varying the CPC concentration factor. The acceptance angles considered in the parameter study are $\theta = 25°$, $\theta = 30°$, $\theta = 35°$ and $\theta = 45°$.

The four main parameters of the study n_{aper}, h_{rec}, C and θ are probed in all combinations to get a comprehensive picture of the entire parameter space and derived field performance metrics. Additionally, to plants with 10 MW at the receiver, also plants with 7.5 MW and 20 MW are investigated. Because the 20 MW field simulation requires at least twice as much computation time, the power variation study contains less parameter combinations than the 10 MW parameter study. The choice of parameter combinations is based on the 10 MW study.

The main metric evaluated for the parameter study is the annual average efficiency that HFLCAL calculates for each subfield (see Eq. (5)). To derive a performance value for the total field the subfield efficiencies are averaged:

$$\epsilon_{\mathrm{opt}} = \frac{\sum_1^{n_{\mathrm{aper}}} \epsilon_{\mathrm{annual}}^{(\mathrm{subfield})}}{n_{\mathrm{aper}}} \tag{9}$$

where n_{aper} is the number of apertures equaling the number of subfields and $\epsilon_{\mathrm{annual}}^{(\mathrm{subfield})}$ is the efficiency of each subfield as given by Eq. (5). This annual average total efficiency will in the following be called optical efficiency since it captures the efficiency contributions from all optical parts of the plant, namely the heliostat field and the CPC (see Eq. (3)).

2.4. Generic receiver-reactor surrogate model and plant performance

The approach described above is limited to the solar concentrator. In this section, it is extended to the plant level, where the solar concentrator is linked to the receiver-reactor. One option to quantify the plant performance is by considering the optical efficiency of the solar concentrator and the efficiency of the receiver-reactor at the respective design point flux density, which is a strong simplification. Alternatively, and more accurately, a time-resolved (here hourly at representative days) analysis of the plant performance can be implemented. The latter approach is used in the following. Thereto, it is necessary to quantify the receiver-reactor performance as a function of the hourly flux density, provided by the solar concentrator.

Instead of evaluating the plant performance of a specific receiver-reactor, a generic receiver-reactor is introduced. In order to parametrize the following results, a surrogate model with a low number of parameters is required. Based on the analysis of published receiver-reactor model performance data, it is assumed, that the flux density dependent efficiency of a receiver-reactor for highly endothermic reactions (favoring temperatures well above 1000 °C) can be reasonably well approximated by shifted sigmoid curves. The efficiency $\epsilon_{\mathrm{rec\_rea}}$ of a generic receiver-reactor as a function of the flux density I is therewith given as:

$$\epsilon_{\mathrm{rec\_rea}}(I) = \max\left(0,\ \frac{2 \cdot \epsilon_{\max}}{1 + \exp(-k(I - I_0))} - \epsilon_{\max}\right) \tag{10}$$

with the fitting parameters efficiency maximum $\epsilon_{\max}$, minium flux density I_0 (below which the efficiency is basically zero), and a growth rate k. By fitting this surrogate model to actual performance data points, the respective fitting parameters are obtained. The max-function is used to avoid negative efficiency values at fluxes below I_0. At the lower end, the performance is limited by this minimum flux density, which can be translated into a minimum receiver-reactor operation temperature (considering only optical losses). For high flux densities the performance converges towards the peak efficiency forming a plateau. At very high flux densities, depending on the actual process and its implementation, the real receiver-reactor performance might drop again, for example due to the shortening of process durations, the increase of heat losses or limitations of other transport mechanisms. As the optical efficiency of the solar concentrator typically decreases with increasing concentration factors, the receiver-reactor performance for flux densities beyond the receiver-reactor efficiency peak is expected to be less relevant for optimal configurations. Therefore, the plateau assumption is considered appropriate for the plant performance evaluation in this study. While the analysis of the surrogate model approach is ongoing work, the good agreement with published performance data as described in 3.2 is a first indicator for a broader applicability. In order to further generalize the analysis as described below, a normalized efficiency is introduced by dividing the efficiency by the maximum efficiency $\epsilon_{\max}$ of the respective receiver-reactor, reducing the required fitting parameters to two. The normalized efficiency is defined by two arbitrary data points, for which the intersection with the abscissa (I_0, 0) and the point at which $\epsilon_{\mathrm{rec\_rea,n}} = 0.5$, namely ($I_{0.5}$, 0.5), are chosen:

$$\epsilon_{\mathrm{rec\_rea,n}} = \frac{\epsilon_{\mathrm{rec\_rea}}}{\epsilon_{\max}} = \frac{2}{1 + (1/3)^{\frac{I - I_0}{\Delta I}}} - 1 \tag{11}$$

with $\Delta I = I_{0.5} - I_0$. This normalized efficiency, defined by only two parameters I_0 and ΔI, is then used to quantify the ratio between the plant efficiency based on an hourly analysis of representative days ($\epsilon_{\mathrm{plant,hourly}}$), and the plant efficiency derived from average and design point values ($\epsilon_{\mathrm{plant,design}}$). The ratio between the two annual efficiency

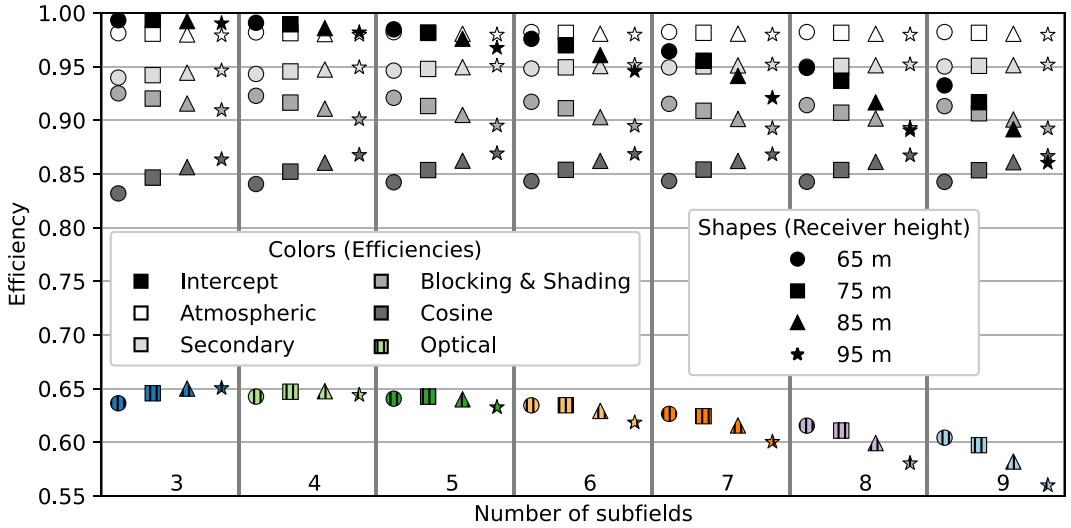

Fig. 3. An excerpt from the results of the parameter study 10 MW design point power. The receiver height is marked by the symbols while the color marks the number of subfields. The concentration factor is set to $C = 2000$ and the CPC acceptance angle to $\theta = 35°$. The optical efficiency is an annual average efficiency as returned by the simulation program HFLCAL and further averaged over the subfields (see Eq. (9)). The different gray values mark the different loss mechanisms implemented in HFLCAL with the colored datapoints being the product of the above resulting in the optical efficiency. The maximum optical efficiency decreases with number of subfields. At low subfield numbers higher towers are more efficient in contrast to high subfield numbers, where the effect is reversed. (For interpretation of the references to color in this figure legend, the reader is referred to the web version of this article.)

estimates, which can be used as a correction factor, is given by:

$$\eta_{\epsilon_{\text{plant}}} = \frac{\epsilon_{\text{plant,hourly}}}{\epsilon_{\text{plant,design}}} = \frac{\sum_{(x,y)} \sum_t w(t) \cdot P(x,y,t) \cdot \epsilon_{\text{rec\_rea,n}}(I(t))}{E_{\text{tot,annual}} \cdot \epsilon_{\text{opt}}(C) \cdot \epsilon_{\text{rec\_rea,n}}(I(C))} \tag{12}$$

In order to avoid detailed field investigations in future initial parametrized plant performance studies, a correlation $\eta^*_{\epsilon_{\text{plant}}}(I_0, \Delta I, C)$ will be provided approximating the correction factor $\eta_{\epsilon_{\text{plant}}}$. With this correlation, with the optical efficiency values determined in this study and with the fitted parameters (I_0, ΔI, $\epsilon_{\max}$) from the generic model (11) for a specific receiver-reactor, the more accurate plant performance estimate can be obtained from the design point value using (see also Section 3.3):

$$\epsilon_{\text{plant,hourly}} \approx \eta^*_{\epsilon_{\text{plant}}} \cdot \epsilon_{\text{plant,design}} = \eta^*_{\epsilon_{\text{plant}}} \cdot \epsilon_{\text{rec\_rea}} \cdot \epsilon_{\text{opt}} \tag{13}$$

3. Results

In this chapter the results of the simulations are presented. Section 3.1.1 gives an overview over all of the results from the parameter study at 10 MW design point power. The influence of the parameters ((i)–(iv) described above) on the optical efficiency and their pairwise relations are the focus of the next sections. Further results of a scaled solar concentrator at high concentration factor are provided to investigate the effect of different parameters on the plant performance. Interpretations for the behavior will be offered, where possible, keeping in mind that the complexity of the inter-dependencies does not permit simple relations. In Section 3.1.4 the optical efficiency is time-resolved by analyzing the varying flux input over the course of the year. The parameters of a generic receiver-reactor surrogate model are calculated in Section 3.2. Based on these results, the correction factors for the annual plant performance estimation are presented in Section 3.3.

3.1. Solar concentrator assessment

3.1.1. Parameter study of the optical efficiency at 10 MW design point power

Fig. 3 shows the contribution of the different efficiencies, calculated as one minus the respective losses (intercept, atmospheric, secondary, blocking & shading and cosine as described in Section 2.2), to the optical efficiency. The displayed set of data points has a fixed concentration factor of 2000 and a CPC acceptance angle of 35°. For every number of subfields four receiver heights above ground are simulated. It is visible that the optical efficiency is increasing with receiver height for three subfields. This behavior turns around at four and more subfields. The largest loss is the cosine loss. Cosine efficiency increases with receiver height, since the angle between the Sun, the heliostats and the receiver is smaller especially at times of high solar input around noon. On the other hand, blocking and shading efficiency decreases, although to a smaller degree, with receiver height which is in part caused by the shadow of the tower. The two effects together lead to the arc pattern in the optical efficiency at each subfield number. Atmospheric efficiency and secondary efficiency do not change at a significant degree neither with receiver height nor with subfield number.

The intercept efficiency is highly dependent on the subfield number. With a subfield number of six and higher it dominates the behavior of the optical efficiency albeit not exhibiting the highest losses. The intercept efficiency decreases significantly with receiver height and with subfield number. At the lowest subfield number the intercept causes almost no loss regardless of the receiver height. The explanation for the dependence on the number of subfields can be inferred from Eq. (7). It shows that at fixed concentration factor the aperture radius must shrink with the root of the number of subfields. At the same time the beam diameter does not change significantly as it is set by the heliostat errors and the sunshape (see Eq. (1)). The result is more spillage and thus decreased intercept efficiency. One possible explanation of the strong height dependence that the intercept exhibits at high subfield numbers could be the widening of the beam diameter with increasing distance between the heliostat and the receiver. Further analysis of this behavior lies out of the scope of this study.

Fig. 4 shows an overview of all 448 data points generated in the parameter study for the 10 MW case. The subfields contribute equally towards the optical efficiency since the design point power is distributed equally over the subfields. The data points are hierarchically sorted by parameter importance which is derived from a correlation study. The most influential parameter, the concentration factor, determines the primary grouping followed by successively less important parameters down to the least significant parameter, the receiver height,

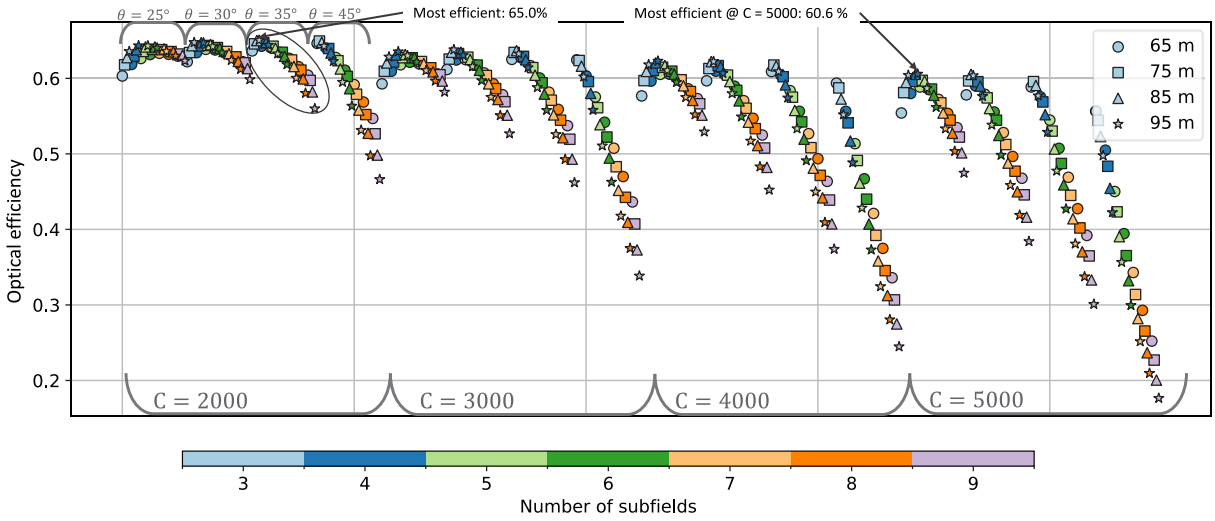

Fig. 4. All data points of the parameter study at 10 MW total design point power from all apertures of the subfields. The parameters varied are the CPC acceptance angle θ, the subfield number n_{aper}, the concentration factor C and the receiver height h_{rec}. The optical efficiency is an annual average efficiency as returned by the simulation program HFLCAL and then averaged over the subfields (see Eq. (9)). (For interpretation of the references to color in this figure legend, the reader is referred to the web version of this article.)

varying between adjacent datapoints. Notably, the concentration factor's importance is not static; as its value increases, it amplifies the impact of the other parameters. The color encodes the number of subfields from 3 (light blue) to 9 (light purple). The individual arcs belong to one CPC acceptance angle each. Different symbols are chosen to represent the four different receiver heights above ground. The entire parameter space covers optical efficiencies from 20% up to 65%.

The color pattern shows that smaller subfield numbers generally lead to higher efficiencies. The highest optical efficiency of 65.0% is achieved for 3 subfields, a 95 m tower with a concentration factor of 2000 and an acceptance angle of 35°. For a concentration factor of 5000, efficiencies of over 60% can still be reached and the corresponding field configuration is shown in Fig. 2. The fields with the highest optical efficiency per concentration factor can be found in Table 1. These 10 MW field configurations are the ones that are considered for the plant simulation in Section 3.3. For 7.5 MW and 20 MW parameter regions that promise high optical efficiencies in particular are sampled. A linear fit to the optical efficiency vs. the concentration factor for all three power levels is given in Table 4 in Appendix.

The comparison with results of other studies is difficult, since there are differences in the design point powers and flux densities, the use of secondary concentrators and the number of apertures. The most relevant studies are the ones by Martinek et al. [5], Brendelberger et al. [10] and Li et al. [6]. The following comparison refers to annual average efficiencies in all cases.

Schmitz et al. [4] reported optical efficiencies of up to 55% for receivers with a design point power between 10 and 600 MW using CPCs. Pitz-Paal et al. [3] reported optical efficiencies of 53.4% at a flux density of 4.6 MW/m^2 and 61.5% at a flux density of 2.9 MW/m^2, both at 10 MW. Martinek et al. [5] reported solar efficiencies of 41.6% for flux densities of 7.4 MW/m^2 at 120 MW and Brendelberger et al. [10] reported solar concentrator efficiencies of about 55% for design point flux densities of 2.5 MW/m^2 at 10 MW. Li et al. [6] reported optical efficiencies of about 56% for a single aperture 40 MW receiver operated at 1600 K, while multi-aperture designs showed lower efficiencies for systems with up to 80 MW. The annual optical efficiencies of over 60% for concentration factors of up to 5000 reported here are therefore considered as a substantial performance improvement.

3.1.2. *Pairwise analysis of parameters with respect to optimal optical efficiency*

The optical efficiency for pairwise combinations of the study parameters can be found in Fig. 5. The black dots mark the results from the simulation while the heatmap in the background is interpolated. For the parameters that are not displayed, the parameter combination that leads to the highest optical efficiency is chosen. The green dot shows the parameter combination with the highest optical efficiency over the entire map. The fact that the highest efficiencies are found at the edge of the parameter region suggests that the design might be further improved by adjusting the parameter range. However, since the study is limited on purpose to concentration factors bigger than 2000 and at least 3 subfields, only adjustments of the receiver height would be eligible.

Fig. 5(a) shows the relation between the optical efficiency, the CPC acceptance angle and the number of subfields. A higher number of subfields generally leads to a lower optical efficiency especially at higher CPC acceptance angles. The CPC acceptance angle links the receiver aperture radius to the entry aperture radius of the CPC, where small acceptance angles lead to big CPC entry apertures so that the spillage decreases while big acceptance angles result in small CPC entrances that increase spillage. The highest efficiencies can be found at low subfield numbers and medium acceptance angles.

The optical efficiency is plotted as a function of CPC acceptance angle and receiver height in Fig. 5(b). The efficiency scale of this figure is much narrower, showing the relatively low influence these parameters have around the peak efficiency. At higher receiver heights and medium acceptance angles the highest efficiencies can be found.

Fig. 5(c) shows that the concentration factor has a higher influence on the optical efficiency than the acceptance angle. In comparison to the color scale of Fig. 5(a), it is visible that the number of subfields has the same magnitude of influence on the optimal optical efficiency, whereas in the overall parameter study (see Fig. 4) the CPC acceptance angle had the second biggest influence. The difference is that the contour plots consider only the maximum optical efficiency, which does not change much with the CPC acceptance angle. This can be seen by comparing the upper end of the θ-arcs in Fig. 4. The acceptance angle only increases the spread of the values over the subfield number which

Table 1
For every heliostat field power level the field configurations that lead to the highest optical efficiency for every concentration factor are given. The spillage is shown as well as the CPC acceptance angle θ, the number of subfields n_{aper} and the receiver height h_{rec}. A linear fit to the optical efficiency vs. the concentration factor for each power level can be found in Table 4 in the Appendix.

Total receiver power [MW]	Optical efficiency	Spillage	Concentration factor	Acceptance angle [°]	Number of subfields	Receiver height [m]
7.5	0.651	0.0081	2000	35	3	75
	0.639	0.0161	3000	30	3	85
	0.625	0.0241	4000	25[a]	3	95[a]
	0.609	0.0444	5000	25[a]	3	95[a]
10	0.650	0.0098	2000	35	3	95[a]
	0.638	0.0145	3000	30	3	95[a]
	0.623	0.0258	4000	25[a]	4	95[a]
	0.606	0.0496	5000	25[a]	4	95[a]
20	0.645	0.0137	2000	45[a]	3	95[a]
	0.627	0.0260	3000	35	4	95[a]
	0.611	0.0316	4000	30	4	95[a]
	0.593	0.0567	5000	30	4	95[a]

[a] Parameter values are at the edge of the probed parameter space showing the direction in which further improvements could potentially be found.

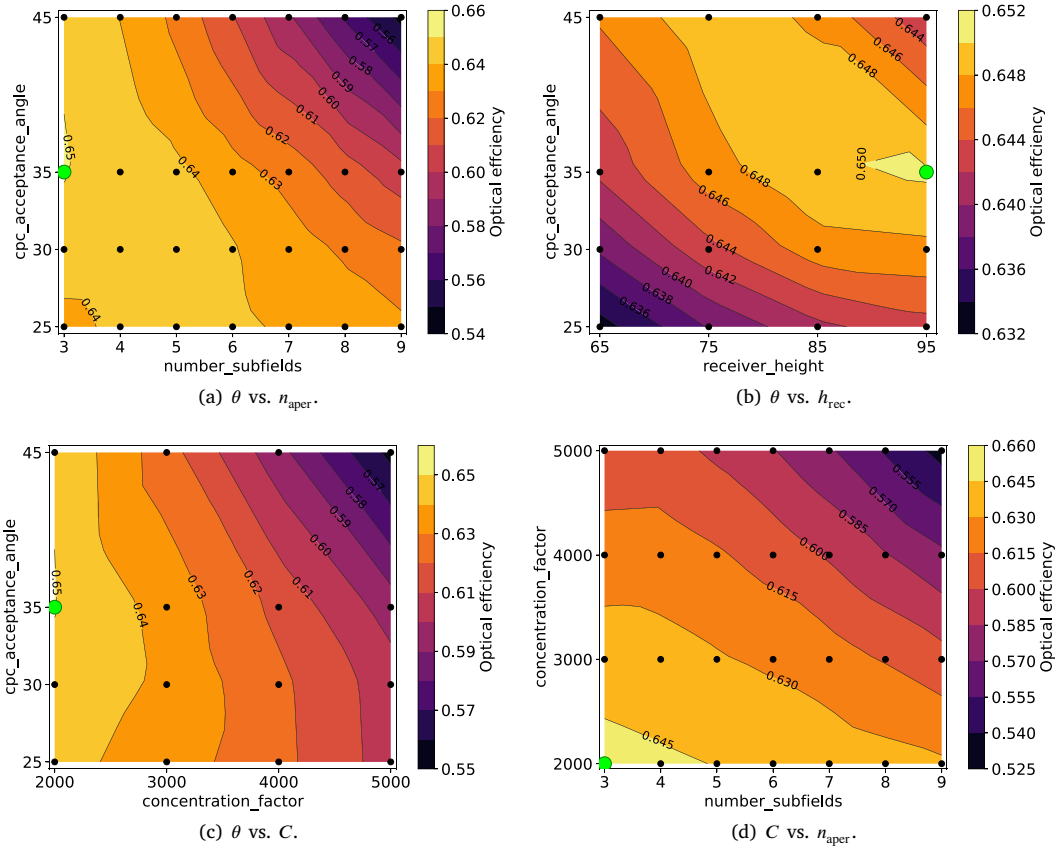

(a) θ vs. n_{aper}. (b) θ vs. h_{rec}. (c) θ vs. C. (d) C vs. n_{aper}.

Fig. 5. Contour plots of the optical efficiency mapped over two parameters respectively. For the parameters that are not displayed, the parameter combination that leads to the highest optical efficiency is chosen. The black dots mark the measured data, from which the heatmap in the background is linearly interpolated. The green dot marks the parameter combination with the highest optical efficiency in the plot. (For interpretation of the references to color in this figure legend, the reader is referred to the web version of this article.)

can also be seen in Fig. 5(a) where the full scale of the colormap is used for the highest acceptance angle of 45°. Furthermore, the shape of the contour lines changes for different concentration factors. At low concentration factors medium acceptance angles produce the best results while at high concentration factors small CPC acceptance angles seem to be more favorable. In a possible extension of the study to higher concentration factors this should be taken into account.

The combination of the two most influential parameters, the concentration factor and the number of subfields, is shown in Fig. 5(d). The figure shows a trend towards higher efficiencies for lower concentration factors and subfield numbers. The slope of the contour lines reveals that at low subfield numbers, the influence of the concentration factor dominates whereas at high subfield number, the number of subfields is most important for determining the optical efficiency.

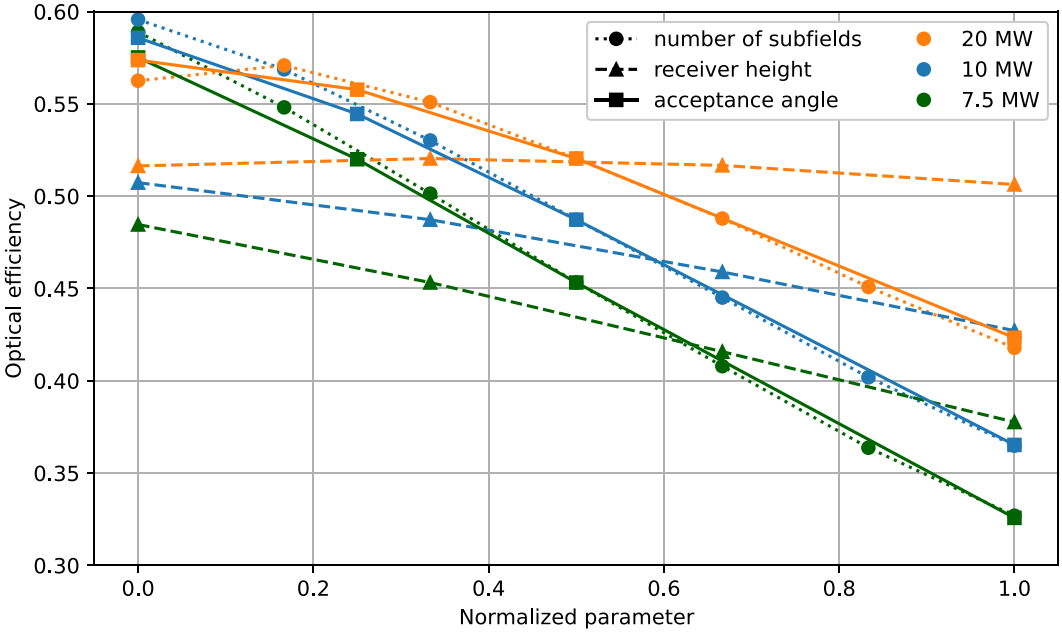

Fig. 6. Optical efficiency at different total design point power levels for a concentration factor of $C = 5000$. The parameter values used are the same as in the parameter study and they are normalized only for visual purposes where 0 corresponds to the lowest parameter value and 1 to the highest respectively. The parameters that are not varied are fixed at $h_{rec} = 75$ m, $\theta = 35°$ and $n_{aper} = 6$. At 20 MW design point power the receiver height has only a minor influence while the number of subfields and acceptance angle show a very similar behavior. The 20 MW concentrators exhibits higher efficiencies at high parameter values whereas at low parameter values the overall highest efficiencies can be found for the 10 MW concentrators. (For interpretation of the references to color in this figure legend, the reader is referred to the web version of this article.)

3.1.3. Design point power variation

Having established the dependence of the optical efficiencies on the chosen parameters at 10 MW, we proceed to investigate how these trends are affected by variations in the receiver's design-point power. A 20 MW solar concentrator (selected due to computational time considerations with a possible extension in the future) and a 7.5 MW concentrator are simulated to enable trends to be inferred. Since high flux solar concentrators are the most interesting for high temperature applications, the concentration factor is set to $C = 5000$ for the power variation. The results are shown in Fig. 6. All other parameters are varied one parameter at a time from a base case in the same steps as in the parameter study. The base case is chosen to be $h_{rec} = 75$ m, $\theta = 35°$ and $n_{aper} = 6$. Normalization of the parameters is only for visualization purposes and happens during post-processing. The plot shows the optical efficiency for a total design point power of 7.5 MW in green, for 10 MW in blue (the parameter study described in Section 3.1.1) and for 20 MW in orange.

The receiver height does not have a significant influence on the efficiency even less so for higher power levels, although it shows the greatest change in behavior with power level. In contrast to that, the number of subfields and the CPC acceptance angle both significantly decrease the efficiency for higher parameters in a similar fashion on every power level. The one difference is that there is a peak in subfield number for the 20 MW concentrator causing the solid and dotted orange line to cross twice. This looks similar to the trend noted by Schmitz et al. [4] that higher subfield numbers become increasingly more efficient for higher design point powers. The highest optical efficiencies can be found for the lowest parameter values. The fact that the 10 MW solar concentrator has the overall highest values is an artifact of the choice of parameters that was derived from the 10 MW parameter study.

This study has been limited to field designs of up to 20 MW total power. To take further advantage of scale-up, higher power levels might need to be considered in a follow-up study. For such a study the most promising parameter ranges are likely to move towards higher subfield numbers and higher receiver heights.

3.1.4. Hourly variation of the flux

In the sections above the focus was on the annual average total optical efficiency, thus the data points are going through two averaging procedures that hide the underlying time-dependence of the solar input. In this section we will look exemplarily at the time series of the flux over three representative days (21st January, 21st March and 21st July) for one field. The chosen field is the configuration with the highest optical efficiency for the highest concentration factor, because high concentration factors are in particular interesting with respect to the receiver-reactor efficiency that we want to calculate in the next section. For the chosen field ($n_{aper} = 4, C = 5000, \theta = 25°, h_{rec} = 95$ m) the single subfield flux as well as the average flux curves are shown in Fig. 7. Of the four subfields only the two in the western half of the heliostat field are plotted. They have a mirrored behavior to the ones in the eastern half as the tower shadow moves over the fields during the day. Averaging over the day leads to the east–west symmetry mentioned in Section 2.1. The flux is calculated by dividing the hourly power that enters the respective apertures through their area: $I(t) = P(t)/A_{aper}$. The aperture area is not time dependent but given by the design point concentration factor and design point power through Eq. (7). The design point flux of 4.86 MW/m^2 is a product of the design point concentration factor of 5000 and the DNI at the design date, the 21st of March at 12:00, of 971.8 W/m^2. Here all subfield curves meet by design. The highest flux values are reached in January since this is the summer on the southern hemisphere, where our simulated plant is placed. All of the curves show a slight asymmetry as there are no fields that directly point to the north or the south (see Fig. 2 for reference).

From the flux time series in Fig. 7 it is evident that most hours during the year have fluxes that fall below the design point flux. Since receiver-reactors typically perform less well at lower flux densities, this negatively impacts the plant efficiency (as can be seen in Fig. 9).

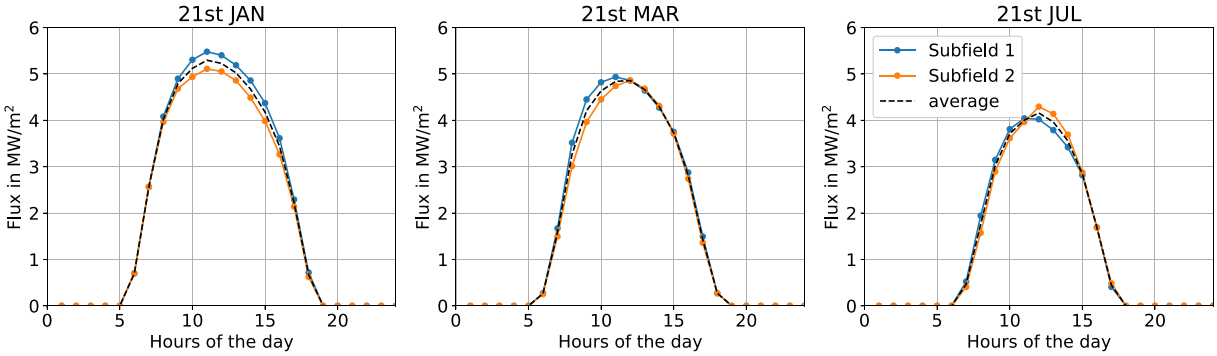

Fig. 7. For the most efficient field for the highest concentration factor ($n_{aper} = 4, C = 5000, \theta = 25°$ and $h_{rec} = 95$ m) the flux entering the apertures is shown time-resolved over the year. All hours of the 21st of January (southern summer), March (southern autumn) and July (southern winter) are displayed. The dashed black curve shows the average over the subfield apertures. Only the first two subfields are displayed as the other two show the mirrored behavior because of the east–west symmetry.

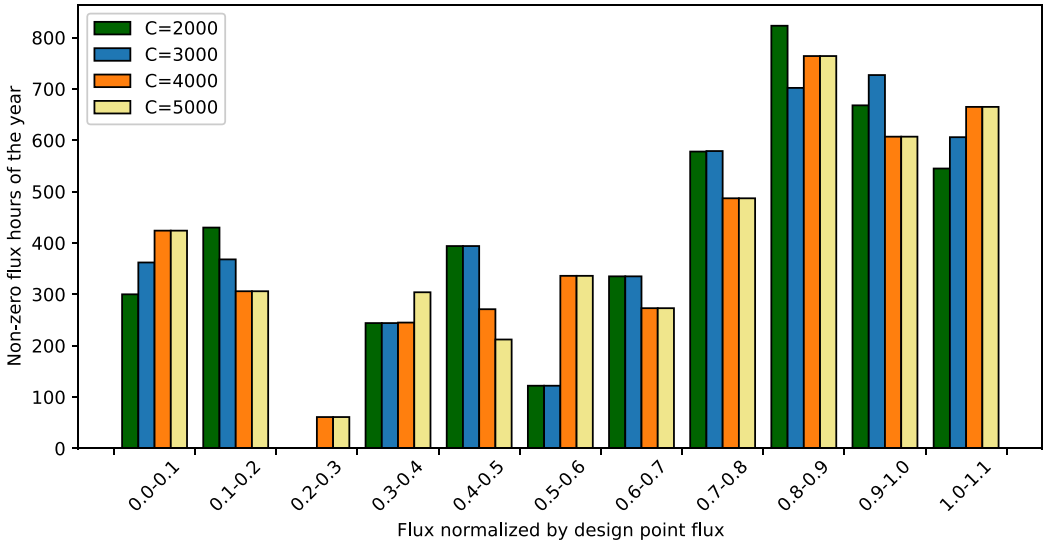

Fig. 8. Average flux histograms of all non-zero flux hours of the most efficient solar concentrators at every concentration factor, the parameters of which can be found in Table 1. The hourly flux data is averaged over the number of subfields and normalized by the design point flux at each concentration factor respectively.

To have a more detailed look on how the hours of the year are distributed over the flux levels, Fig. 8 shows a histogram of all non-zero flux hours of the most efficient heliostat field configurations at every concentration factor as given in Table 1. For each configuration the flux is first averaged over the number of subfields. As HFLCAL provides flux data for all hours on the 21st of each month, these are first replicated as many times as there are days in the month. Then the fluxes are normalized by the respective design point flux of the field. At this point hours with zero flux are removed. Afterwards they are summed up in the histogram in bins that correspond to the fraction of design point flux reached. From this it is again apparent that the majority of hours are below design point flux with very similar percentages in between the different field configurations: 85.0%, 85.0%, 86.4% and 87.7% for concentration factors of 5000, 4000, 3000 and 2000 respectively. In order to investigate the plant performance, the hourly flux densities are decisive and will be considered for the plant performance estimates in Section 3.3, after the evaluation of the receiver-reactor surrogate model.

3.2. Generic normalized receiver-reactor surrogate model

A simple generic surrogate model is proposed in Section 2.4 to approximate the normalized receiver-reactor efficiency dependence on the flux density at the aperture. The resulting performance approximations for different receiver-reactor systems are shown in Fig. 9 and are compared to data points from detailed receiver-reactor model studies.

The blue dots labeled "R2Mx" are derived from Figure 9 of Brendelberger [15] for input flux densities between 2 MW/m^2 and 5 MW/m^2 for the system with the highest plant efficiency. The other design and operational parameters of the receiver-reactor like temperature and pressure are kept fixed. The blue dashed curve shows the corresponding fitted receiver-reactor surrogate model (Eq. (11)). The fitted parameters are $I_0 = 0.45$ MW/m^2, $I_{0.5} = 1.75$ MW/m^2 and $\epsilon_{max} = 0.185$. A very good match of the fitted curve with the data points can be observed ($R^2 > 0.99$). Results from a different receiver-reactor model for zinc oxide reduction (from Pitz-Paal et al. [3]) are included to show the broader applicability of the approach. Thereto, data points from Figure 2a in Pitz-Paal et al. [3] are extracted for flux densities between 0.5 MW/m^2 and 4.2 MW/m^2 for an receiver-reactor with an aperture area of 0.5 m^2 and labeled "Zinc". The corresponding fitted orange curve describes the data points well ($R^2 > 0.99$), though with slightly larger deviations compared to the "R2Mx" case. The normalized receiver-reactor description (Eq. (11)) is therefore considered a simple but sensible surrogate model for high-temperature receiver-reactors that will be used to ana-

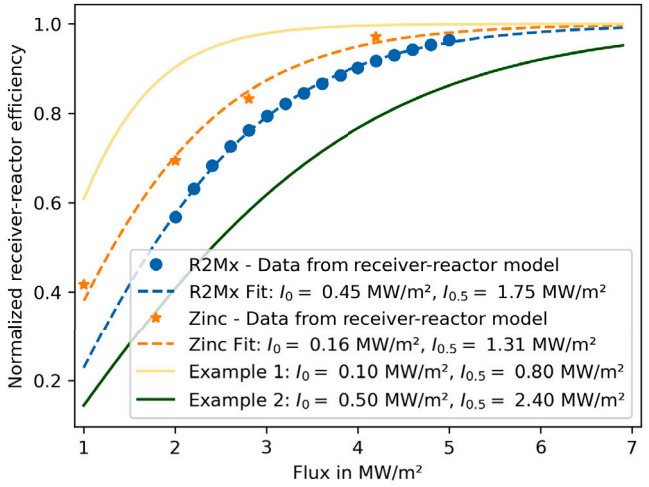

Fig. 9. Performance characteristics of normalized receiver-reactors efficiencies. The data points indicate values from previously published receiver-reactor performance models - in particular R2Mx by Brendelberger [15] and a zinc receiver-reactor by Pitz-Paal et al. [3]. The dashed lines are fitted generic receiver-reactor surrogate models and the solid lines two additional examples with different behavior. The fitted I_0 and $I_{0.5}$ values are shown in the legend. (For interpretation of the references to color in this figure legend, the reader is referred to the web version of this article.)

lyze the performance of generic receiver-reactors in combination with solar concentrators. As shown below, this can be used further to refine plant performance predictions.

To indicate how the characteristic curves vary with the parameters I_0 and $I_{0.5}$, two additional generic receiver-reactors are depicted exemplarily in Fig. 9. The first one, example 1, with $I_0 = 0.1$ MW/m^2 and $I_{0.5} = 0.8$ MW/m^2, represents a receiver-reactor that starts operating at low flux densities and reaches half of its maximum efficiency at 0.8 MW/m^2. The second one, example 2, with $I_0 = 0.5$ MW/m^2 and $I_{0.5} = 2.4$ MW/m^2 describes a system, that converges relatively slowly to its maximum efficiency and requires a high minium flux density of 0.5 MW/m^2.

3.3. Plant performance correction factor

The purpose of the following section is to investigate the yearly performance of a solar thermochemical plant, combining a solar concentrator with a parametrized generic receiver-reactor. In particular, we quantify the error resulting from design point plant performance estimations in comparison to the more accurate assessment based on an hourly analysis. Design point estimations are used in literature when detailed flux conditions of the solar concentrator are not available and when a dedicated solar field simulation is out of scope (for example in [13–15]). With the information presented below, a correction factor can be derived to compensate for the corresponding performance prediction error in order to more accurately estimate the performance.

The correction factor is given by the ratio $\eta_{\epsilon_{\text{plant}}}$ between $\epsilon_{\text{plant,hourly}}$ and $\epsilon_{\text{plant,design}}$ (see Eq. (12)). It depends on the design point concentration factor of the solar field C and the receiver-reactor characteristics given by the parameters I_0 and $I_{0.5}$ for the generic normalized receiver-reactor surrogate model. Note that the parameter ϵ_{max} is not relevant for this analysis, justifying the use of the normalized receiver-reactor performance definition. As only $I_{0.5} > I_0$ values lead to meaningful results, $\eta_{\epsilon_{\text{plant}}}$ is calculated as a function of I_0 and ΔI instead. Since one is in particular interested in the most efficient solar concentrator designs, the hourly distributions of the best performing 10 MW concentrators (see Table 1) are used. The correction factor is exemplarily shown in Fig. 10 for $C = 2000$ and $C = 5000$.

The correction factor plots in Fig. 10 show values between 0.7 and 0.99. The values decrease with decreasing design point concentration factors and increasing values of I_0 and ΔI. The latter values indicate cases where the receiver-reactor favors higher flux densities and reaches the performance plateau later.

In order to make the correction factor more easily accessible for other plant studies $\eta^*_{\epsilon_{\text{plant}}}$ (see also Eq. (12)) is provided, which is a fit with $R^2 = 0.97$ to the most effective solar concentrators (for C between 2000–5000, I_0 between 0.1–0.6 MW/m^2, ΔI between 0.5–1.9 MW/m^2 and a total receiver design point power of 10 MW):

$$\begin{aligned}\eta^*_{\epsilon_{\text{plant}}}(I_0, \Delta I, C) = &-2.545 \times 10^{-4} \cdot I_0/(\text{kW/m}^2) \\ &- 8.221 \times 10^{-5} \cdot \Delta I/(\text{kW/m}^2) \\ &+ 7.647 \times 10^{-5} \cdot C + 4.127 \times 10^{-8} \cdot I_0/(\text{kW/m}^2) \cdot C - 7.397 \times 10^{-9} \cdot C^2 \\ &+ 8.312 \times 10^{-1} \end{aligned} \quad (14)$$

The above can be used to reassess yearly plant performance predictions using [15] as an example. The yearly average R2Mx plant efficiency in the cited study is calculated based on average and design point values considering a parametrized receiver-reactor model. It should be noted that the described plant model in [15] makes assumptions about waste heat usage and additional energy demands of the periphery which are not considered here. The highest plant efficiency is obtained for a design point concentration factor of 4600 and for a receiver-reactor with a characteristic profile as shown in Fig. 9. This leads to a correction factor of 0.89 indicating a 11% overestimation of the performance. As in the cited study the optical efficiency was approximated with values significantly below the optical efficiency values obtained for the best performing solar concentrators identified in this study (53.4% at 4.6 MW/m^2 [3] vs. 60.6% at 4.86 MW/m^2 in this study), the optical performance potential at high concentration factors was significantly underestimated compared to the results of this more detailed analysis. As the effects almost balance each other out by chance at $C = 4600$ in total a slight underestimation (2%) of the plant efficiency for the particular receiver-reactor design from the referenced study [15] is obtained. The refined analysis indicates that the peak performance is shifted to higher design point concentration factors, motivating to explore such solar concentrators in further studies.

The findings of the study support a time-resolved investigation, at least hourly at representative days, to obtain more accurate yearly performance predictions. The presented correction factor function (Eq. (14)) can be used, if a field optimization tool is not available or if the related effort is out of scope for the particular study. It can be inserted into Eq. (13) together with ϵ_{opt} from Table 4 and $\epsilon_{\text{rec\_rea}}$ (Eq. (10)). Further plant performance optimization potential can be expected, if the performance characteristic of the particular receiver-reactor is directly considered in a field optimization study using a tool like HFLCAL. Due to the high computational costs, this would be done after an initial evaluation of parametrized receiver-reactor models, as described above, once the preselection has converged to a limited number of specific receiver-reactor designs.

4. Conclusion and outlook

A solar concentrator layout study for multi-aperture central receiver designs is presented. In particular, systems that provide flux densities above 2 MW/m^2 are investigated as such high flux densities are required in receivers for high-temperature applications, for example in receiver-reactors for thermochemical cycles, and the available information in literature for such systems is limited.

The software HFLCAL is used for the simulation of the solar heliostat fields with central receivers and secondary concentrators. The software allows to calculate the annual efficiency, while optimizing the number and positions of the heliostats in combination with the receiver tilt angle for maximum optical efficiency. In a parameter study the receiver

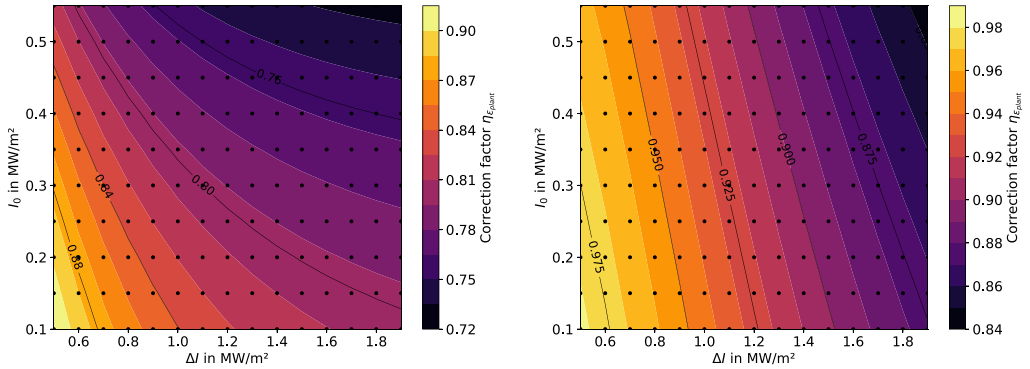

(a) $C = 2000$. (b) $C = 5000$.

Fig. 10. The correction factor is given by $\eta_{\epsilon_{plant}}$ and can be used to compensate design point based plant performance estimates. The parameters ΔI and I_0 from the normalized generic receiver-reactor surrogate model cover a wide range of different receiver-reactor performance characteristics (see Eq. (11)).

height above ground, the acceptance angle of the CPC, the number of subfields and the design point concentration factor at the aperture are examined with respect to their influence on the optical efficiency. Additionally, the performance at different design point power levels are evaluated. In order to conduct the over 500 heliostat field optimizations, a Python script is developed to automate the access of HFLCAL and streamline the evaluation of the simulation results.

At 10 MW scale, solar concentrators with optical efficiencies above 60% for design point concentration factors up to $C = 5000$ are identified. The optical efficiency reacts most strongly to the concentration factor, the acceptance angle and the number of subfields in descending order. The receiver height has a smaller effect. Since the most efficient systems are obtained for the highest receiver heights considered in the parameter study, it seems likely that the maximum optical efficiencies can be further increased, if higher receivers are included in further studies. Also, the extension to larger concentration factors seems particularly interesting when considering the performance with a linked high-temperature receiver-reactor, since they promise higher receiver-reactor efficiencies at higher flux densities. The power variation study identifies the number of subfields and the CPC acceptance angle as important parameters in solar concentrator designs with increasing total power.

An important goal of this study is to identify and characterize promising solar concentrators for high-temperature receivers and in particular receiver-reactors and to make these results accessible for other plant studies (combined system of solar concentrator and receiver-reactor). Thereto, instead of focusing on a specific receiver-reactor, a generic receiver-reactor surrogate model is introduced which is used to evaluate parametrized plant performances at an hourly basis and annual values. Since the flux density provided by the solar concentrator is below the design point value for the vast majority of hours during the year, the plant performance is usually well below the value obtained by just considering the annual average efficiency of the solar concentrator and the design point efficiency of the receiver-reactor. The ratios between the values obtained by the hourly analysis to the ones obtained by the design point performance are quantified and a parametrized correction factor is provided. This approach circumvents a dedicated detailed solar concentrator study while providing a good approximation of a performance estimate based on an hourly analysis. Further improvement options for follow-up studies are described.

CRediT authorship contribution statement

Hanna Lina Pleteit: Writing – review & editing, Writing – original draft, Visualization, Software, Investigation, Formal analysis, Conceptualization. **Stefan Brendelberger:** Writing – review & editing, Writing – original draft, Visualization, Supervision, Software, Formal analysis, Conceptualization. **Peter Schwarzbözl:** Writing – review & editing, Software, Methodology. **Malou Großmann:** Software, Methodology. **Martin Roeb:** Writing – review & editing. **Christian Sattler:** Writing – review & editing, Funding acquisition, Conceptualization.

Funding source

This work was partially funded by the German Federal Ministry for Economic Affairs and Climate Action under the funding code Redox3D (03EE5124A). Furthermore, the authors gratefully acknowledge the funding provided by the Deutsches Zentrum für Luft- und Raumfahrt e.V.'s basic funding for the research project "SOLHYKO". The authors are responsible for the content of this publication.

Declaration of competing interest

The authors declare that they have no known competing financial interests or personal relationships that could have appeared to influence the work reported in this paper.

Appendix

See Tables 2–4.

Table 2
Table of the receiver aperture radii in meters for different concentration factors and subfield numbers.

Number of apertures ↓/concentration factor →	2000	3000	4000	5000
3	0.739	0.603	0.522	0.467
4	0.640	0.522	0.452	0.405
5	0.572	0.467	0.405	0.362
6	0.523	0.427	0.369	0.330
7	0.484	0.395	0.342	0.306
8	0.452	0.369	0.320	0.286
9	0.427	0.348	0.302	0.270

Table 3
Linear fit to the optical efficiency of the most efficient fields at each design point power as given in Table 1. The fit can be used as a simplified characterization of the solar concentrator behavior for concentration factors between 2000 and 5000.

Total receiver power [MW]	Linear fit	R^2 value
7.5	$\epsilon_{opt} = -1.47 \times 10^{-5} \cdot C + 6.81 \times 10^{-1}$	0.994
10	$\epsilon_{opt} = -1.40 \times 10^{-5} \cdot C + 6.80 \times 10^{-1}$	0.996
20	$\epsilon_{opt} = -1.72 \times 10^{-5} \cdot C + 6.79 \times 10^{-1}$	0.999

Table 4
Quadratic fit to the spillage of the most efficient fields at each design point power as given in Table 1. The fit can be used as a simplified characterization of the solar concentrator behavior for concentration factors between 2000 and 5000.

Total receiver power [MW]	Quadratic fit	R^2 value
7.5	$\epsilon_{spil} = 1.73 \times 10^{-9} \cdot C^2 - 9.61 \times 10^{-8} \cdot C$	0.979
10	$\epsilon_{spil} = 2.13 \times 10^{-9} \cdot C^2 - 1.16 \times 10^{-6} \cdot C$	0.966
20	$\epsilon_{spil} = 1.52 \times 10^{-9} \cdot C^2 + 3.22 \times 10^{-6} \cdot C$	0.952

References

[1] J.T. Tran, K.J. Warren, S.A. Wilson, C.L. Muhich, C.B. Musgrave, A.W. Weimer, An updated review and perspective on efficient hydrogen generation via solar thermal water splitting, Wiley Interdiscip. Rev. Energy Environ. 13 (4) (2024) e528, http://dx.doi.org/10.1002/wene.528, URL: https://wires.onlinelibrary.wiley.com/doi/full/10.1002/wene.528.

[2] W.C. Chueh, C. Falter, M. Abbott, D. Scipio, P. Furler, S.M. Haile, A. Steinfeld, High-flux solar-driven thermochemical dissociation of CO2 and H2O using nonstoichiometric ceria, Science 330 (6012) (2010) 1797–1801, http://dx.doi.org/10.1126/science.1197834.

[3] R. Pitz-Paal, N.B. Botero, A. Steinfeld, Heliostat field layout optimization for high-temperature solar thermochemical processing, Sol. Energy 85 (2) (2011) 334–343, http://dx.doi.org/10.1016/j.solener.2010.11.018, URL: https://www.sciencedirect.com/science/article/pii/S0038092X10003580.

[4] M. Schmitz, P. Schwarzbözl, R. Buck, R. Pitz-Paal, Assessment of the potential improvement due to multiple apertures in central receiver systems with secondary concentrators, Sol. Energy 80 (1) (2006) 111–120, http://dx.doi.org/10.1016/j.solener.2005.02.012, URL: https://elib.dlr.de/22305/1/SE_2006_111_Schmitz.pdf.

[5] J. Martinek, M. Channel, A. Lewandowski, A.W. Weimer, Considerations for the design of solar-thermal chemical processes, Sol. Energy (132) (2010).

[6] L. Li, B. Wang, J. Pye, R. Bader, W. Wang, W. Lipiński, Optical analysis of a multi-aperture solar central receiver system for high-temperature concentrating solar applications, Opt. Express 28 (25) (2020) 37654–37668, http://dx.doi.org/10.1364/OE.404867, URL: https://opg.optica.org/oe/fulltext.cfm?uri=oe-28-25-37654&id=444106.

[7] A. Segal, M. Epstein, Comparative performances of 'Tower-Top' and 'Tower-Reflector' central solar receivers, Sol. Energy 65 (4) (1999) 207–226, http://dx.doi.org/10.1016/S0038-092X(98)00138-8, URL: https://www.sciencedirect.com/science/article/pii/S0038092X98001388.

[8] A. Boretti, S. Castelletto, S. Al-Zubaidy, Concentrating solar power tower technology: present status and outlook, Nonlinear Eng. 8 (1) (2019) 10–31, http://dx.doi.org/10.1515/nleng-2017-0171.

[9] P. Schramek, D.R. Mills, Multi-tower solar array, Sol. Energy 75 (3) (2003) 249–260, http://dx.doi.org/10.1016/j.solener.2003.07.004, URL: https://www.sciencedirect.com/science/article/pii/S0038092X03002548.

[10] S. Brendelberger, A. Rosenstiel, A. Lopez-Roman, C. Prieto, C. Sattler, Performance analysis of operational strategies for monolithic receiver-reactor arrays in solar thermochemical hydrogen production plants, Int. J. Hydrog. Energy 45 (49) (2020) 26104–26116, http://dx.doi.org/10.1016/j.ijhydene.2020.06.191, URL: https://www.sciencedirect.com/science/article/pii/S0360319920323764.

[11] S. Zoller, E. Koepf, D. Nizamian, M. Stephan, A. Patané, P. Haueter, M. Romero, J. González-Aguilar, D. Lieftink, E. de Wit, S. Brendelberger, A. Sizmann, A. Steinfeld, A solar tower fuel plant for the thermochemical production of kerosene from H2O and CO2, Joule 6 (7) (2022) 1606–1616, http://dx.doi.org/10.1016/j.joule.2022.06.012, URL: https://ars.els-cdn.com/content/image/1-s2.0-S2542435122002860-mmc7.pdf.

[12] Daniel Potter, jin-soo Kim, Yen Chean Soo Too, Sahan Trushad Wickramasooriya Kuruneru, Optimisation of multi-aperture falling particle cavity receivers and heliostat fields, in: Asia - Pacific Solar Research Conference, 2020, URL: https://www.researchgate.net/publication/350750927_Optimisation_of_Multi-aperture_Falling_Particle_Cavity_Receivers_and_Heliostat_Fields.

[13] A. Weber, J. Grobbel, M. Neises-von Puttkamer, C. Sattler, Swept open moving particle reactor including heat recovery for solar thermochemical fuel production, Sol. Energy 266 (2023) 112178, http://dx.doi.org/10.1016/j.solener.2023.112178, URL: https://www.sciencedirect.com/science/article/pii/S0038092X23008125.

[14] C. Falter, V. Batteiger, A. Sizmann, Climate impact and economic feasibility of solar thermochemical jet fuel production, Environ. Sci. Technol. 50 (1) (2016) 470–477, http://dx.doi.org/10.1021/acs.est.5b03515.

[15] S. Brendelberger, R2Mx plant model for solar thermochemical hydrogen production at MW scale, Int. J. Hydrog. Energy 91 (2024) 1407–1421, http://dx.doi.org/10.1016/j.ijhydene.2024.10.050, URL: https://www.sciencedirect.com/science/article/pii/S0360319924042411.

[16] P. Schwarzbözl, R. Pitz-Paal, M. Schmitz, Visual HFLCAL - A software tool for layout and optimisation of heliostat fields, in: T. Mancini, R. Pitz-Paal (Eds.), Proceedings of SolarPACES, 2009, URL: https://elib.dlr.de/60308/.

[17] P.L. Leary, J.D. Hankins, User's Guide for MIRVAL: A Computer Code for Comparing Designs of Heliostat-Receiver Optics for Central Receiver Solar Power Plants, Technical Report, Sandia National Lab. (SNL-CA), Livermore, CA (United States), 1979, http://dx.doi.org/10.2172/6371450, URL: https://www.osti.gov/biblio/6371450.

[18] W.A. Landman, A. Grobler, P. Gauche, F. Dinter, Incidence angle effects on circular Gaussian flux density distributions for heliostat imaging, Sol. Energy 126 (2016) 156–167.

[19] G. Johnston, On the analysis of surface error distributions on concentrated solar collectors, J. Sol. Energy Eng. 117 (4) (1995) 294–296, http://dx.doi.org/10.1115/1.2847843, arXiv:https://asmedigitalcollection.asme.org/solarenergyengineering/article-pdf/117/4/294/5711801/294_1.pdf.

[20] A. Neumann, A. Witzke, S.A. Jones, G. Schmitt, Representative terrestrial solar brightness profiles, in: J.B. Pearson, J.B. Pearson (Eds.), Solar Engineering 2002, American Society of Mechanical Engineers, New York, NY, 2002, pp. 325–333, http://dx.doi.org/10.1115/SED2002-1069.

[21] H.C. Hottel, A simple model for estimating the transmittance of direct solar radiation through clear atmospheres, Sol. Energy 18 (2) (1976) 129–134, http://dx.doi.org/10.1016/0038-092X(76)90045-1, URL: https://www.sciencedirect.com/science/article/pii/0038092X76900451.

[22] W.T. Welford, R. Winston, Optics of Nonimaging Concentrators. Light and Solar Energy, Academic Press Incorporated,New York, NY, 1978, URL: https://www.osti.gov/biblio/5380269.

[23] A. Pfahl, M. Randt, C. Holze, S. Unterschütz, Autonomous light-weight heliostat with rim drives, Sol. Energy 92 (2013) 230–240, http://dx.doi.org/10.1016/j.solener.2013.03.005, URL: https://www.sciencedirect.com/science/article/pii/S0038092X13001023.

[24] M. Burisch, X. Olano, M. Sanchez, A. Olarra, C. Villasante, D. Olasolo, R. Monterreal, R. Enrique, J. Fernández, Scalable heliostat calibration system (SHORT) - Calibrate a whole heliostat field in a single night, AIP Conf. Proc. 2033 (1) (2018) 040009, http://dx.doi.org/10.1063/1.5067045, arXiv:https://pubs.aip.org/aip/acp/article-pdf/doi/10.1063/1.5067045/13992595/040009_1_online.pdf.

[25] G. Zhu, J. Sment, C. Turchi, M. Gordon, R. Brost, R. Mitchell, D. Kesseli, T. Farrell, M. Muller, K. Armijo, et al., Heliostat Consortium Annual Report: 2024, Technical Report, National Renewable Energy Laboratory (NREL), Golden, CO (United States), 2024, http://dx.doi.org/10.2172/2475372, URL: https://www.osti.gov/biblio/2475372.

[26] J. Dersch, P. Schwarzbözl, T. Richert, Annual yield analysis of solar tower power plants with GREENIUS, J. Sol. Energy Eng. 133 (3) (2011) http://dx.doi.org/10.1115/1.4004355.